

Alkali Mono-Pnictides: A New Class of Photovoltaic Materials by Element Mutation


Yu Kumagai^{1,*}, Seán R. Kavanagh^{2,3}, Issei Suzuki⁴, Takahisa Omata⁴, Aron Walsh,³
David O. Scanlon² and Haruhiko Morito¹

¹*Institute for Materials Research, Tohoku University, 2-1-1 Katahira, Aoba-ku, Sendai, 980-8577, Japan*

²*Thomas Young Centre and Department of Chemistry, University College London, 20 Gordon Street, London WC1H 0AJ, United Kingdom*

³*Thomas Young Centre and Department of Materials, Imperial College London, Exhibition Road, London SW7 2AZ, United Kingdom*

⁴*Institute of Multidisciplinary Research for Advanced Materials, Tohoku University, 2-1-1 Katahira, Aoba-ku, Sendai, Japan*

 (Received 20 May 2023; revised 31 July 2023; accepted 14 August 2023; published 3 October 2023)

Selenium (Se) has been studied for over 140 years as the first solid-state solar cell, yet it has only achieved a maximum power conversion efficiency of 6.5%. To improve the efficiency, we propose derivative structures via element mutation. Specifically, we replace Se with Group 15 pnictogens (Pn = P, As, Sb) and fill the interchain space with alkali metals ($M = \text{Li, Na, K, Rb, Cs}$). Our calculations reveal that the band gaps of MPn span the optimal range for solar absorption. We find that NaP, composed of earth-abundant elements, has excellent properties as a solar cell absorber, including a slightly indirect band gap, high optical absorption coefficient just above the absorption onset, light electron and hole effective masses, and ambipolar dopability. However, carrier capture calculations show that P vacancies may limit its photovoltaic performance. Therefore, we propose solutions to reduce P vacancies through chemical potential control. Finally, we present preliminary results of NaP powder sample growth; this reveals a direct band gap of 1.66 eV, close to the predicted value of 1.62 eV. MPn represents a new class of absorber to rival other emerging photovoltaic technologies.

DOI: [10.1103/PRXEnergy.2.043002](https://doi.org/10.1103/PRXEnergy.2.043002)

I. INTRODUCTION

In 1873, Willoughby Smith reported that solid selenium (Se) exhibited photoconductivity [1]. Three years later, Adams and Day demonstrated the first solid-state solar cell using Se [2]. Since then, Se has been investigated as a photovoltaic material [3]. Among various types of crystal structure, the trigonal phase (t -Se) with infinite helical Se chains on a hexagonal lattice [Fig. 1(a)] records the best solar cell performance [3]. Indeed, t -Se is known to have a high absorption coefficient over 10^4 cm^{-1} just above the absorption onset. However, the best power conversion efficiency reaches only 6.5% [4], which is low compared to >22% in commercialized photovoltaic materials, such as Si, CdTe, GaAs, CuInSe₂, and hybrid

perovskites [5]. One contributing factor is the larger band gap of 1.8 eV [3] compared to the optimal value around 1.3–1.5 eV estimated from the Shockley-Queisser (SQ) limit [6], which already decreases the radiative efficiency limit from 33.7% to 27.2% [6]. In addition, wide band gap materials tend to be much less defect tolerant, by providing wider energetic regions for deep defect levels to arise, which can decrease solar efficiency through nonradiative recombination [7,8].

Substituting elements while maintaining charge neutrality, often referred to as element mutation (see, for example, Ref. [9]), is a common practice in the search for new materials. Examples are II-VI semiconductors, such as ZnSe, which are obtained from Group 14 semiconductors (e.g., Si) by element mutation [Fig. 1(b)]. The Zn^{2+} site can be further mutated to +1 and +3 cations, resulting in I-III-VI semiconductors, e.g., CuInSe₂. Here, we propose a way to extend the element mutation technique. Instead of simply substituting one element with two, while retaining the average oxidation state, we introduce ions into the vacant sites within the structure and mutate the elements while preserving overall neutral charge.

*yukumagai@tohoku.ac.jp

Published by the American Physical Society under the terms of the [Creative Commons Attribution 4.0 International](https://creativecommons.org/licenses/by/4.0/) license. Further distribution of this work must maintain attribution to the author(s) and the published article's title, journal citation, and DOI.

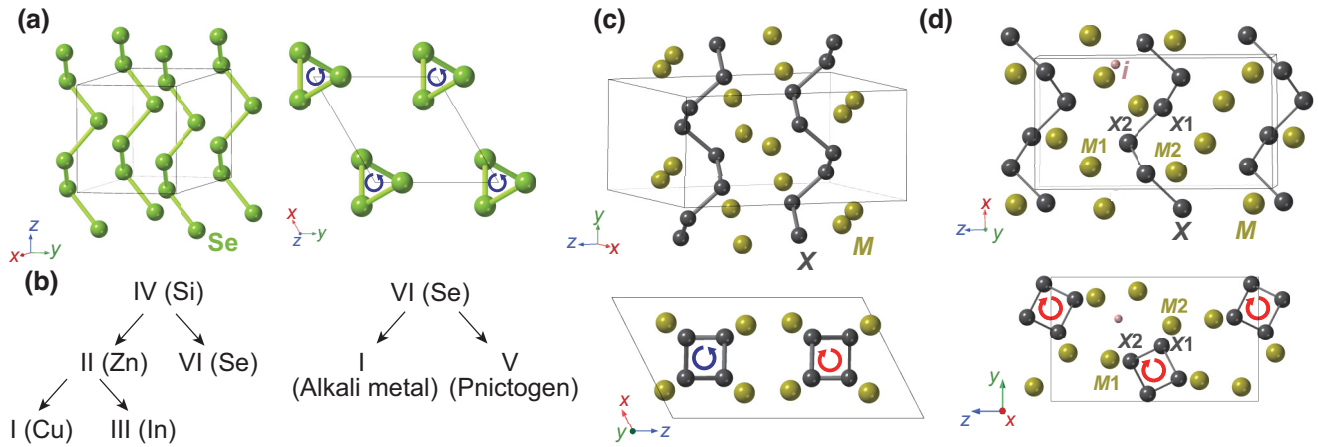


FIG. 1. (a) Crystal structure of trigonal Se. (b) Schematics of the element mutation from the Group 14 and Group 16 elemental semiconductors. Crystal structures of (c) monoclinic and (d) orthorhombic alkaline mono-pnictides. Blue and red circled arrows depict the helical chain rotation directions from the back of the paper to the front. In (d), inequivalent sites and an interstitial site (*i*) considered in the point-defect calculations are also illustrated. Interstitial site in *o*-NaP is located at (0.938, 0.667, 0.675) in fractional coordinates.

To retain the chainlike structures in *t*-Se, we consider Group 15 pnictogens as anions, due to their ability to cateenate (i.e., self-bond in the form of low-dimensional ring, layer, and chainlike motifs) [10]. The cations are then intercalated between the chains to maintain a charge balance [see Figs. 1(c) and 1(d)]. Such alkali mono-pnictides (MPn , $M = \text{Li, Na, K, Rb, Cs}$; $Pn = \text{P, As, Sb}$) have indeed been partly synthesized, as shown in Fig. 2(a).

One advantage of the MPn composition is that the physical properties can be optimized by changing the cation-anion combinations or synthesizing their alloys. For instance, the band gap is controllable within a range of optimal band gaps for solar cells, as shown later. Another advantage is the electrostatic interactions between cations and anion chains: contrary to the weak van der Waals interactions between the Se chains in *t*-Se, the cations should attract the anion chains more strongly, which results in greater stability.

In this study, we performed first principles calculations on the phase stability and optoelectronic properties of MPn compounds to investigate their potential as photovoltaic materials. It is found that a series of MPn compounds cover the appropriate band gap range for solar cells and exhibit relatively strong optical absorption onsets and low electron and hole effective masses. We also calculated the point defects in NaP, a representative of MPn composed of non-toxic and earth-abundant elements, because point defects generally dominate the photovoltaic performance. Our calculations reveal that P vacancies (V_P , where V means a vacancy) have relatively low formation energies and show deep levels, which should be detrimental to photovoltaic efficiency based on the Shockley-Read-Hall (SRH) theory for nonradiative recombination [11,12]. Indeed, calculations of nonradiative carrier capture rates reveal that the

carrier recombination by V_P is likely to be significant. To reduce V_P concentrations, we propose to control the Fermi level by adjusting growth conditions and/or introducing dopants. To verify our calculations, we synthesized NaP and measured its direct band gap using a diffuse reflection measurement. Our experiment shows that the observed direct band gap is 1.66 eV, which closely matches the calculated direct band gap of 1.62 eV.

II. RESULTS AND DISCUSSION

A. Physical properties of alkali mono-pnictides

Experimentally, MPn is known to crystallize in the monoclinic phase (*m*- MPn) with space group $P2_1/c$ [Fig. 1(c)] or the orthorhombic phase (*o*- MPn) with space group $P2_12_12_1$ [Fig. 1(d)]. Although there are two anion chains in both unit cells, the spiral handedness is different, as shown in Figs. 1(c) and 1(d); two chains rotate in opposite directions in the monoclinic phase, while they rotate in the same direction in the orthorhombic phase. However, the local structures are similar. For example, two inequivalent cation sites are coordinated by five and six anions, respectively, in both phases. The cycles are different between MPn and *t*-Se; the anion chains in *m*- and *o*- MPn have a fourfold screw rotation [Figs. 1(c) and 1(d)], while the Se chains in *t*-Se have a threefold screw rotation [Fig. 1(a)], resulting in the space group $P3_121$.

Figures 2(a) and 2(b) show the experimentally observed phases and the calculated total energy differences between the two phases, respectively. We used the HSE06 functional in all calculations because it is a reliable method for predicting semiconductor properties (see Sec. IV for details). The ionic radii generally increase as one moves down the periodic table [13]. As the ratio

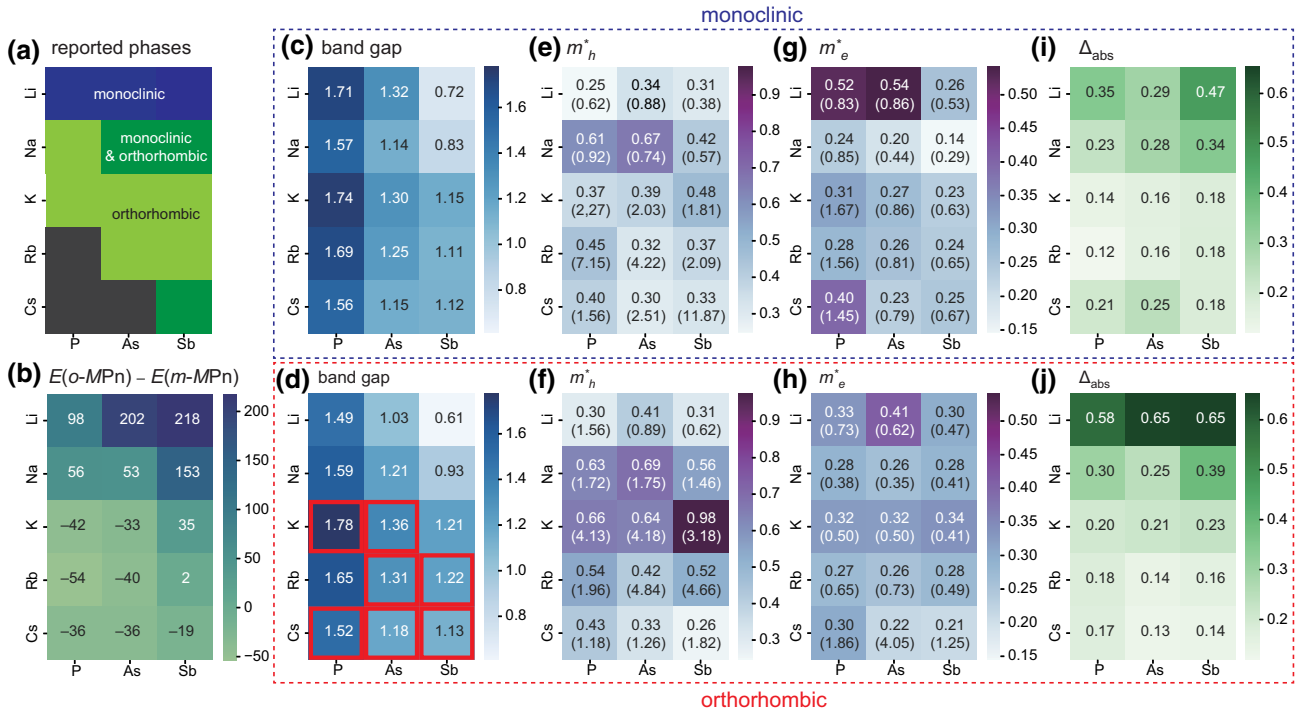


FIG. 2. (a) Experimentally reported phases. Dark gray color indicates that neither monoclinic nor orthorhombic phases are reported. (b) Total energy of the orthorhombic phase relative to that of the monoclinic phase for each composition ($E(o\text{-MPn}) - E(m\text{-MPn})$), in meV/f.u. Positive (negative) values indicate that the monoclinic (orthorhombic) phases are more stable. (c),(d) Calculated band gaps in eV; (e),(f) minimum hole effective masses (m_h^*); (g),(h) minimum electron effective masses (m_e^*); and (i),(j) optical absorption onsets in eV (see text for details). Top panels (c),(e),(g),(i) are the results for the monoclinic phases, while bottom panels (d),(f),(h),(j) are those for the orthorhombic phases. Effective masses are in units of the electron rest mass. In (c),(d), direct bands are surrounded by red squares. In (e)–(h), mean effective masses are also shown in brackets. All the calculations were performed using the HSE06 functional.

of cation to anion ionic radii decreases, the monoclinic phase becomes more stable. This is mainly because the interchain space is slightly smaller in $m\text{-MPn}$. In fact, the volumes of $m\text{-MPn}$ are smaller than those of $o\text{-MPn}$ for all cation-anion combinations (see Table S2 within the Supplemental Material [14]).

In experiments, NaSb and CsSb have been synthesized in both phases. In contrast, our calculations show that the monoclinic phase is more stable by 153 meV/formula unit (f.u.) in NaSb, while the orthorhombic phase is more stable by 19 meV/f.u. in CsSb. These results suggest that it may be possible to synthesize other phases that have not been reported before, with an energy difference of a few tens of eV/f.u.

CsP and RbP have not been reported experimentally. However, RbP has been calculated in a rocksalt structure in the Materials Project Database (MPD) but is extremely unstable (0.99 eV/atom above the hull). On the other hand, CsAs has been reported experimentally [15] but its structure does not contain As chains but As_3 rings. Theoretically, we have calculated the convex hulls for these CsP, CsAs, and RbP compositions using

the total energies calculated with HSE06 and found that their monoclinic phases were stable, as shown in Fig. 3. In fact, $o\text{-CsAs}$ is 42 meV/f.u. more stable than the experimentally reported hexagonal phase [16]. Therefore, their synthesis via growth condition optimization is likely possible.

Figures 2(c) and 2(d) show the calculated band gaps. The differences between the two polymorphs are relatively small in each case, with a mean absolute difference of only 0.08 eV. The band gaps are in the range of 0.61–1.78 eV, encompassing the optimal band gap range for solar absorption around 1.3–1.5 eV in the SQ limit. The gap decreases significantly as the anion element is shifted down the pnictogen group from P to As to Sb due to the reduced ionization potential of the anions; the average band gaps of phosphides, arsenides, and antimonides are 1.63, 1.22, and 1.00 eV, respectively. On the other hand, the cation species do not have a large effect because they are spectator ions with a small contribution to the band edges [17], as shown in Sec. II B. The calculated Wannier-Mott exciton binding energies for MPn are also provided in Table S4 within the Supplemental Material [14], ranging from 0.02 eV for $o\text{-LiSb}$ to 0.43 eV for $o\text{-KP}$.

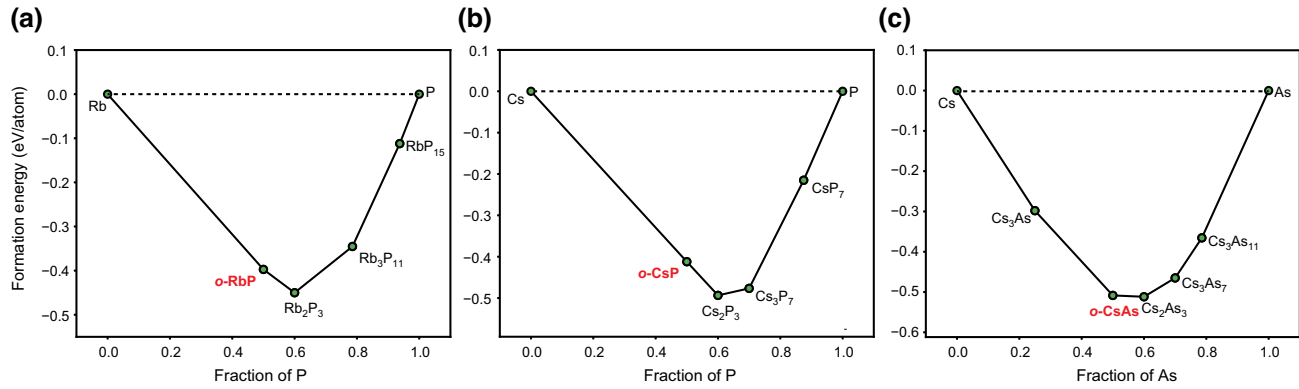


FIG. 3. Thermodynamic convex hulls for (a) Rb-P, (b) Cs-P, and (c) Cs-As binary systems. Newly identified orthorhombic *MPn* compounds are highlighted in red.

B. Electronic structures of earth-abundant *o*-NaP

Because *o*-NaP is composed of earth-abundant elements and has an adequate *fundamental* band gap (1.59 eV), effective electron and hole masses, and absorption sharpness (see below), we now turn our focus to its electronic structure. We would like to emphasize that our calculated lattice constants match our experimental values, as shown in the Supplemental Material. Figures 4(a)–4(d) show its band structure as well as partial charge densities, Brillouin zone, density of states (DOS), and optical absorption spectrum, respectively. Those of the other compositions in both phases are also shown in Figs. S1–S6 within the Supplemental Material [14], showing similar qualitative behavior in terms of bonding and DOS orbital contributions. Therefore, the behavior shown for NaP is a representative example for the other compositions and phases.

The valence bands are divided into three regions. The deep-lying energy region from -15 to -7 eV, denoted as region I, is mainly composed of P $3s$ orbitals, as shown in Figs. 4(a) and 4(d). Significant band dispersion is seen in the k_x direction, which is parallel to the anion chain direction in real space [see Fig. 1(d)] and reflects the strong intrachain $3s$ σ -bonding interaction, while it is almost flat in the k_y and k_z directions. The middle region from -6 to -3 eV (region II) and the upper region from -3 to 0 eV (region III) consist mainly of the bonding states between P $3p$ orbitals and lone-pair orbitals pointing to free space, respectively [Fig. 4(a)]. Although the conduction bands are not so clearly distinguished, the lower part of the conduction bands is composed of intrachain antibonding P $3sp$ orbitals. As shown in Figs. 4(c), S3, and S4 within the Supplemental Material [14], the anion n - s and $-p$ orbitals ($n=3, 4$, and 5 for P, As, and Sb, respectively) mainly constitute the band edge states. Negligible orbital contributions to the band edges are found for the M^+ ions, as expected, which behave as spectator ions with no covalent

interactions [17]. This electronic structure is similar to that of *t*-Se and is also found in chalcogenides, such as As_2Se_3 [18,19].

The valence band maximum (VBM) is located on the Γ -Y line, while the conduction band minimum (CBM) is at the Γ point. Indeed, these two are slightly displaced in many *MPn* phases, except for K, Rb, and Cs compounds in the orthorhombic phases (Figs. S1 and S2 in the Supplemental Material [14]). Such slightly indirect-gap (“pseudodirect”) characteristics can be favorable for solar cell applications because they inhibit the band-to-band radiative carrier recombination. For example, the radiative recombination coefficient of direct-gap *p*-GaAs is on the order of $10^{-10} \text{ cm}^3 \text{ s}^{-1}$ at room temperature [20], which is much larger than that of Si, on the order of $10^{-15} \text{ cm}^3 \text{ s}^{-1}$ [21]. Rashba splitting is also known to cause the pseudodirect characteristics, e.g., in the highly efficient perovskite solar cell absorbers [22].

The minimum hole (m_h^*) and electron (m_e^*) effective masses are tabulated in Figs. 2(e)–2(h). In general, the *MPn* compounds show smaller m_h^* and m_e^* than $1m_e$, where m_e is the unit of the electron rest mass, with $m_h^* > m_e^*$ in general, which is typical of semiconductors. Here, this can be ascribed to the weaker interactions of the lone-pair p orbitals comprising the VBM versus the more dispersive intrachain antibonding sp interactions at the CBM. Significant carrier mass anisotropy is witnessed across all *MPn*, with low m_h^* and m_e^* along the anion chains but heavy masses in the interchain directions. However, the anisotropy depends strongly on the system. The extreme case is the hole effective mass in *m*-CsSb, where the minimum and average hole masses are 0.33 and 11.87, respectively. In such cases, control of the crystal orientation is essential for practical applications. The effective masses are generally sensitive to the crystal structures. For example, the m_h^* of NaP is reduced to about half when the structure is changed from the orthorhombic to the monoclinic phase.

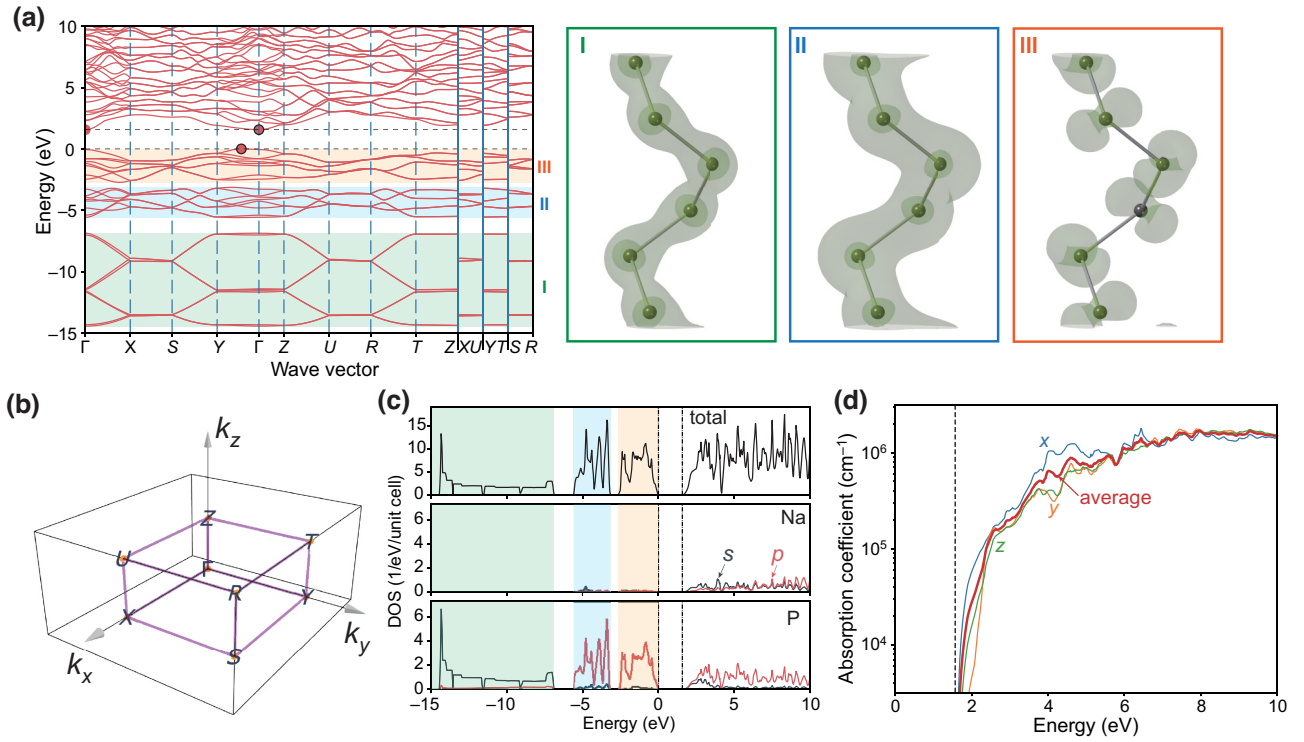


FIG. 4. (a) Electronic band structure, (b) Brillouin zone, (c) total and element-projected DOS, and (e) optical absorption spectrum of *o*-NaP. Valence bands in (a),(c) are color coded into three regions. Partial charge densities calculated from the pseudowavefunctions at regions I, II, and III are also illustrated. Isosurface is set to 60% of the maximum in each case. Band path in (a) is shown in (b) with purple lines. Atom-projected DOS were obtained by summing the DOS for the same element sites in the primitive unit cell.

Figure 4(d) shows the optical absorption coefficient of *o*-NaP. Those of the other compositions in both phases are shown in Figs. S5 and S6 within the Supplemental Material [14]. Since the valence and conduction bands consist of common anion orbitals, high optical absorption is found, especially along the chain direction. Such a steep rise is typical of high-performance photovoltaic materials (e.g., GaAs and hybrid perovskites) [23].

We define the optical gaps as the energies at which the absorption spectra first reach 10^4 cm^{-1} and denote the differences between the optical and fundamental gaps as Δ_{abs} , which is related to the steepness of the optical absorption spectra [24]. Direct-gap compounds, e.g., *o*-CsAs, tend to have smaller Δ_{abs} , but for solar cell applications, indirect-gap materials may be more favorable. Therefore, the indirect materials with smaller Δ_{abs} , such as *m*-RbP, are suitable for use in solar cells.

C. Defect properties of NaP

Figures 5(a) illustrates the chemical potential diagram of the Na-P binary system, whereas Figs. 5(b) and 5(c) display the point defect formation energies under Na- and P-rich conditions, respectively. Irrespective of the growth conditions, the dominant native defects with low formation

energies are Na and P vacancies (V_{Na} and V_{P}), indicating that ionic compensation via Schottky disorder dominates the defect chemistry. Under P-rich conditions, *o*-NaP exhibits *p*-type behavior, while under Na-rich conditions, it shows more insulating behavior. This tendency is comparable to other phosphide semiconductors, such as Zn_3P_2 [25] and ZnSnP_2 [26], despite the difference in phosphorus oxidation states.

The defect and carrier concentrations are determined using the charge neutrality condition [26]. In calculating the carrier concentration at 300 K, we assume that the defects are created at a sintering temperature of 725 K [27], but we keep the defect concentrations fixed during quenching, while allowing for variation of charge states, following the “frozen defect approximation” [26]. Under P-rich conditions, the equilibrium hole concentration is sufficiently high (approximately 10^{18} cm^{-3}), for use in *p*-*n*-junction photovoltaic architectures [28].

The highest achievable Fermi level is set by the energy level where the negatively charged defect formation energy reaches zero. In *o*-NaP, the Fermi level is capped by V_{Na} , even under Na-rich conditions, but it is only 0.21 eV away from the CBM, where the donor concentrations are 7×10^{17} and $4 \times 10^{14} \text{ cm}^{-3}$ at $T = 725$ and 300 K, respectively. Hence, weak *n*-type doping could be achievable if donor dopants were available.

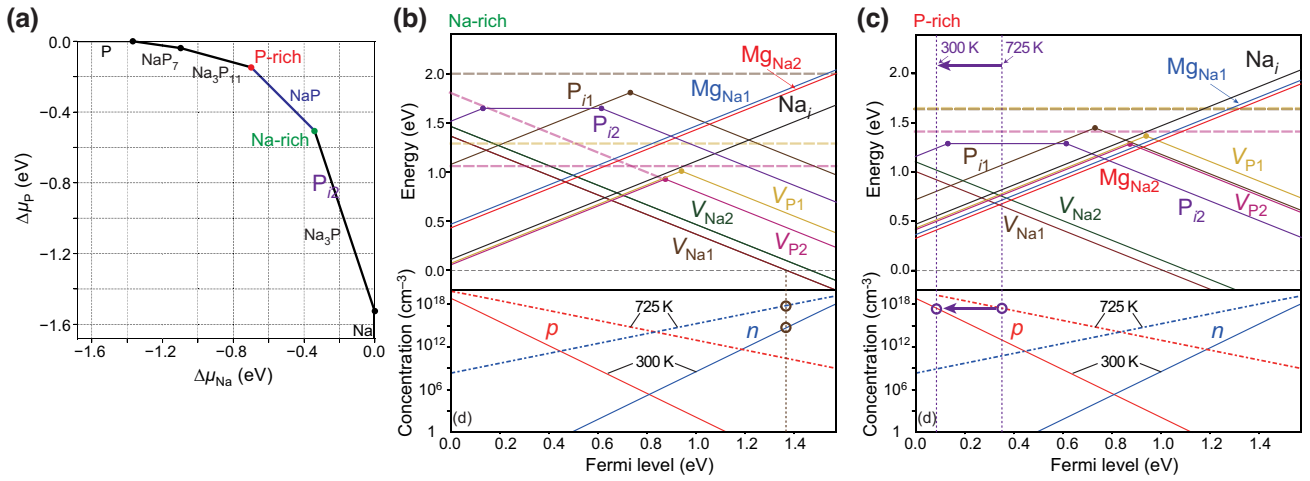


FIG. 5. (a) Na-P chemical potential diagram. (b),(c) Defect formation energies in NaP under (b) Na-rich and (c) P-rich conditions, as designated by green and red dots in (a), respectively. Carrier concentrations at $T = 725$ and 300 K are also shown in (b),(c). The formation energies of metastable neutral V_{P1} , V_{P2} and P_i are also indicated by bold dashed lines.

Divalent cations that preferentially occupy Na sites are favorable as donor-type dopants because the cation orbitals are not involved in the band edge states, and so are expected to act as resonant donors without perturbing the carrier mobilities. We examine Mg impurities because it is a Group II cation adjacent to Na on the periodic table. Figures 5(b) and 5(c) show that Mg dopants function as single shallow donors, but their formation energies are high, necessitating the use of nonequilibrium doping techniques.

V_P and interstitial P (P_i) show ambipolar characteristics accompanying large atomic variations between different charge states. Consequently, the neutral charge states are never thermodynamically stable, i.e., they show negative- U behavior [29]. The effective U values of a defect D with charge q (D^q), calculated by

$$U_{\text{eff}} = E_f[D^{q-1}] + E_f[D^{q+1}] - 2E_f[D^q],$$

where $E_f[D^q]$ means the defect formation energy of D^q , are -0.56 , -0.26 , and -0.38 eV for V_{P1} , V_{P2} , and P_i , respectively.

Based on the SRH expression, nonradiative electron-hole recombination becomes significant when the charge transition levels are located near the center of the band gap [30]. Because V_P show lower formation energies and their charge transition levels are placed in the middle of the gap, V_P could significantly impact solar cell performance. To examine V_P , we compare the local atomic structures before and after the introduction of V_{P1} in Figs. 6(a)–6(d). The results for V_{P2} are shown in Fig. S7 within the Supplemental Material [14]. In the “fully ionized” $+1$ charge state, a covalent bond is formed between two P atoms located next to V_P [Fig. 6(b)]. This bond has a deep energy level that is lower than the valence band maximum [Fig. 6(e)].

In this way, the vacancy is eliminated through recombination of the terminated P chains, which can be seen as a self-healing function. When the charge state is 0 or -1 , however, one or two electrons localize at the vacancy site, and the P chains terminate with a partially or fully occupied lone-pair orbital that exists in the energy gap [Figs. 6(c)–6(f)]. These types of structural reconstructions and resultant negative- U behavior are known to occur at dangling bonds in lone-pair chalcogenides and pnictides and are often termed valence alternation [31,32].

Figures 7(a) and 7(b) show the configuration coordinate diagrams (CCDs) for the $-1/0$ and $0/+1$ charge state transitions of V_{P1} . As a consequence of the very different local structure of V_{P1}^{+1} from those of V_{P1}^0 and V_{P1}^{-1} , the mass-weighted displacement, Q (see Sec. IV B for details), of the equilibrium position at $q = +1$ is approximately twice that at $q = -1$, taking the geometry of the neutral charge state as a reference.

Figure 7(c) displays the nonradiative capture coefficients as a function of temperature, where C_n^q is the capture coefficient of carrier type n [=electron (e) or hole (h)] trapped by defects with charge q . The capture rates for the $-1/0$ transitions are moderate ($C_e^0 = 10^{-10} \text{ cm}^3 \text{ s}^{-1}$ and $C_h^{-1} = 10^{-9} \text{ cm}^3 \text{ s}^{-1}$ at $T = 300$ K), while those of the $0/+1$ transitions are significantly higher (both C_e^{+1} and C_h^0 are $10^{-7} \text{ cm}^3 \text{ s}^{-1}$ at $T = 300$ K). As depicted in Fig. 7(c), the total capture coefficient, C_{total} , can be calculated by assuming steady-state conditions with negligible carrier reemission as [33]

$$C_{\text{total}} = \frac{C_e^0 + C_h^0}{1 + (C_h^{-1}/C_e^0) + (C_e^{+1}/C_h^0)},$$

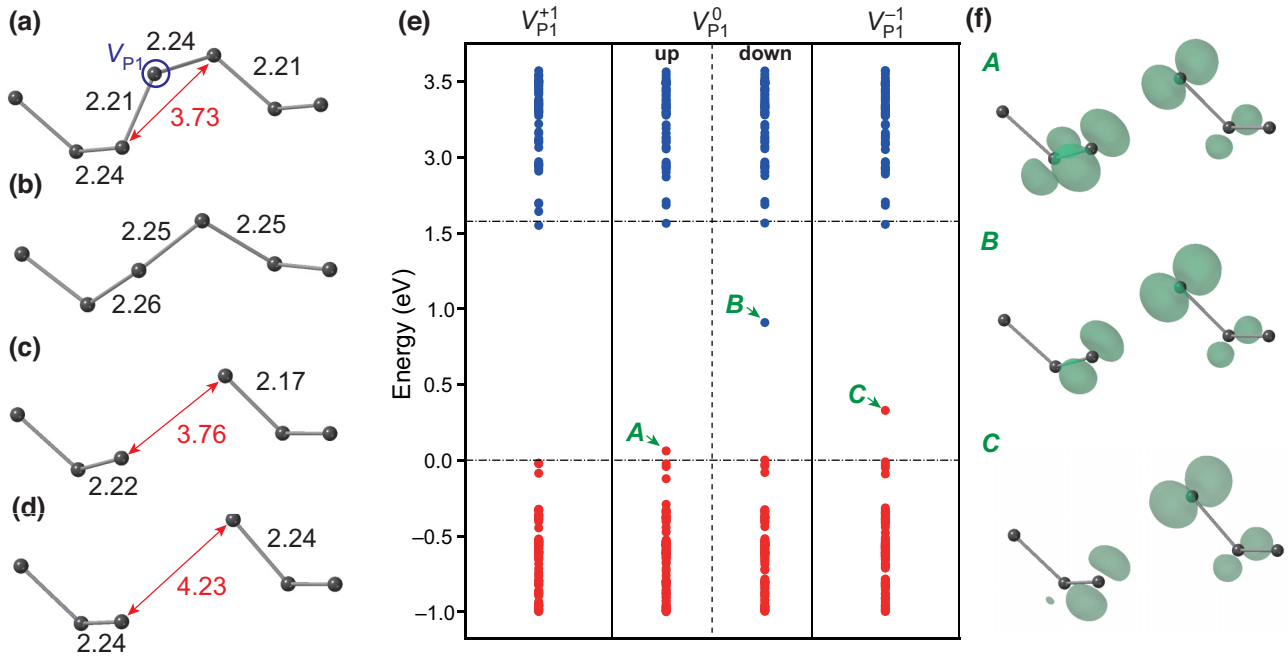


FIG. 6. Atomic structures of the phosphide chains in (a) perfect *o*-NaP and near V_{P1} in (b) +1, (c) 0, and (d) -1 charge states. Distances are given in Å. (e) Single-particle electron levels in the supercell models for V_{P1} , and (f) squared wavefunctions denoted in (e). Isosurfaces are set to 40% of the maximum in each case.

which is notably high and primarily dominated by the 0/+1 transitions. Therefore, the phosphide vacancies are predicted to be detrimental to the performance of photovoltaic applications.

D. Strategies to avoid phosphide vacancies

The concentration of V_P under P-rich conditions is $9 \times 10^{16} \text{ cm}^{-3}$ at $T = 725 \text{ K}$. To decrease V_P , it is straightforward to increase the phosphide chemical potential (μ_P) during sample growth. Although NaP is in equilibrium with Na_3P_{11} under P-rich conditions [Fig. 5(a)], inhibiting the growth of competing phases and/or growing the

samples with high phosphorus partial pressures can further increase μ_P . However, increasing μ_P is not enough to reduce the V_P concentrations. For example, as shown in Fig. 8, even with an increase of μ_P by 0.15 eV ($\delta\mu_P = 0 \text{ eV}$, see Sec. IV A for details), which can be achieved by equilibrating with a phosphorus substance, the V_P concentration at $T = 725 \text{ K}$ is reduced to only $4 \times 10^{16} \text{ cm}^{-3}$. This is a consequence of the fact that the downshift in the self-consistent Fermi level upon increasing μ_P acts to counter the increase in V_P formation energy.

One strategy is to lower the growth temperature. For instance, by lowering the growth temperature to 500 K, the V_P concentration can be reduced to $4 \times 10^{13} \text{ cm}^{-3}$.

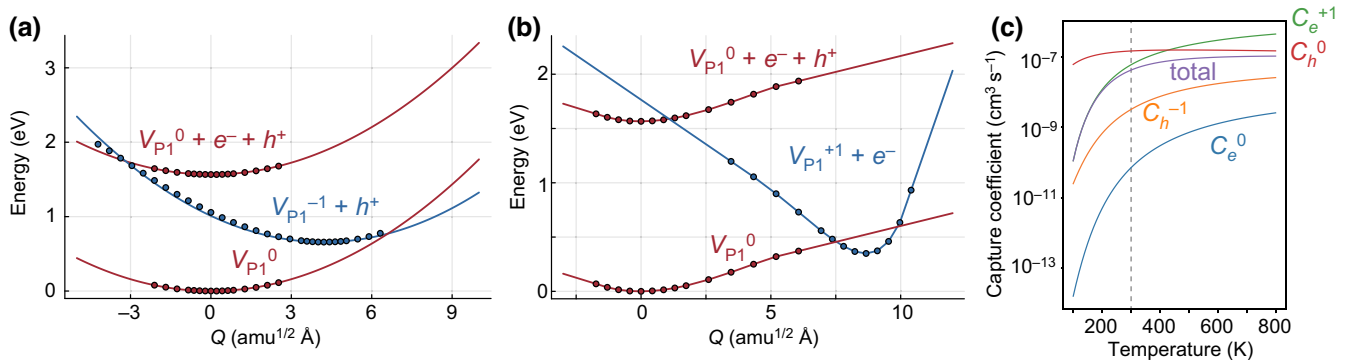


FIG. 7. Configuration coordinate diagrams for (a) -1/0 and (b) 0/+1 charge state transitions of V_{P1} in NaP. (c) Nonradiative capture coefficients of V_{P1} as a function of temperature.

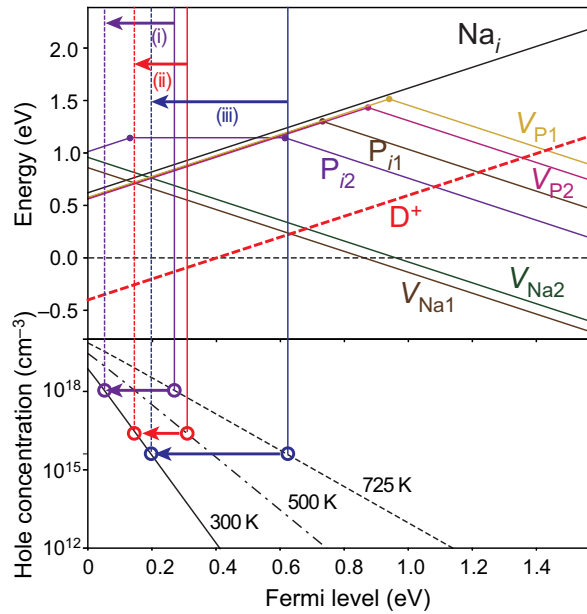


FIG. 8. Defect formation energies in NaP under the $\Delta\mu_P = 0$ eV condition (see text for details). Additionally, the single donor (D^+) formation energy is also shown, which corresponds to a defect concentration of $3 \times 10^{20} \text{ cm}^{-3}$ at 725 K. Lower panel displays hole concentrations as a function of temperature and Fermi level. Solid vertical lines represent the equilibrium Fermi levels at growth temperatures of (i) 725 K and (ii) 500 K without doping, and (iii) 725 K with donor doping, while dashed lines represent those after quenching to 300 K. Circles show the hole concentrations under the three conditions, while arrows indicate the change in Fermi level.

Another approach is to adjust the Fermi level by introducing *donor* dopants. For example, if we introduce single donors (e.g., Mg dopants at Na sites) at a concentration of $3 \times 10^{20} \text{ cm}^{-3}$, the equilibrium Fermi level is raised to 0.62 eV at 725 K, which results in a decrease of V_P concentrations to $1 \times 10^{14} \text{ cm}^{-3}$. However, it should be noted that these two approaches result in a decrease in hole concentration. Therefore, it is crucial to strike a balance between the hole and V_P concentrations.

E. Synthesis of *o*-NaP and measurement of its optical absorption spectrum

To preliminarily verify the potential of NaP as a solar cell material, we synthesized its powder and measured its band gap. By heating Na and P at 873 K in the SUS reaction container, P in the upper crucible fully evaporated and reacted with Na in the lower crucible. A slightly bluish shiny ingot like silicon was produced, as shown in the inset in Fig. 9. The obtained sample was identified as single-phase orthorhombic NaP from the results of powder x-ray diffraction (XRD; see Fig. S8 within the Supplemental Material [14]). No secondary phases, such as Na_3P or P, were detected. The sample weight change before and after

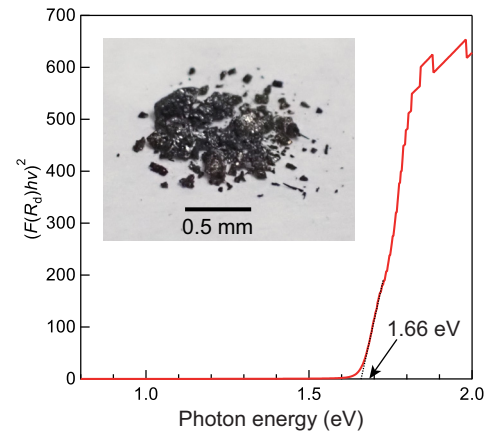


FIG. 9. $(F(R_d)h\nu)^2$ plot of powdered NaP as a function of photon energy obtained using diffuse reflection spectroscopy (see text for details). Inset shows the obtained sample before pulverization.

heating confirmed that NaP with a molar ratio of 1:1 was generated by reacting P vapor and Na melt.

Figure 9 shows the $(F(R_d)h\nu)^2$ plot of *o*-NaP, obtained from diffuse reflection spectroscopy. Here, $F(R_d)$ is the Kubelka-Munk function [34], h is Planck's constant, and ν is the photon frequency. The point where the extrapolated line meets the axis is used to determine the direct band gap of 1.66 eV, which is well reproduced by the calculated direct band gap (1.62 eV).

III. CONCLUSIONS

We propose improving the efficiency of solid selenium (Se), the first solar cell absorber, by using an alternative element mutation technique to explore a new phase space. Because Se is a Group 16 element solid with a chainlike catenation structure, we suggest replacing Se with Group 15 pnictogens ($\text{Pn} = \text{P}, \text{As}, \text{Sb}$) and filling the interchain space with alkali metals ($M = \text{Li}, \text{Na}, \text{K}, \text{Rb}, \text{Cs}$). Some of this family have indeed been synthesized in two different crystal structures. The calculated band gaps of MPn encompass the optimal energy range for solar absorption.

We also find that NaP, which is composed of earth-abundant elements, has excellent properties as a solar cell absorber, including strong light absorption to generate charge carriers and electronic band dispersion to transport them. Carrier capture analysis shows that the presence of P vacancies may introduce a performance bottleneck, but we propose solutions that involve manipulating the atomic and electronic chemical potentials. Finally, NaP sample growth and characterization reveal a direct band gap of 1.66 eV, close to the predicted value. Our study suggests that MPn represents a promising new class of photovoltaic materials.

Finally, we also would like to emphasize that our proposed element mutation technique could be applied to alternative systems, allowing the identification of novel

potentially stable materials, thus offering a new route to the design of materials in general.

IV. METHODS

A. Computational details

The first-principles calculations were performed using the projector augmented-wave (PAW) method [35,36] implemented in VASP [37]. The PAW data sets used in this study are tabulated in Table S1 within the Supplemental Material [14]. We adopted the HSE06 hybrid DFT functional [38] in the framework of the generalized Kohn-Sham scheme [39] because it could typically predict semiconductor band gaps of less than 2.0 eV with good accuracy [40].

For structure optimization and band structure calculations, the k -point sampling densities were set to 2.5 \AA^{-1} . Band paths were determined using seekpath [41] with a mesh spacing of 0.025 \AA^{-1} . The force convergence was set to 5 meV/\AA . We used the same calculation conditions for DOS, optical absorption spectra, and band-averaged effective mass tensors as in our previous research [16,24]. Note that this study does not consider the effects of indirect optical absorptions. The cutoff energies were set to 520 and 400 eV for calculations with and without lattice constant relaxation, respectively.

B. Details of point defect calculations

For the point defect calculations in orthorhombic NaP (o -NaP), the lattice constants were fixed at those in the pristine structure relaxed with HSE06. To increase the accuracy of the carrier capture rates, a large $4 \times 4 \times 2$ supercell composed of 512 atoms was adopted. The reciprocal space was then sampled only with the Γ point.

For the defect charge states, we extended the terminal defect charges to achieve an even number of electrons to ensure that all the defect orbitals could have paired electrons. For example, we calculated -1 , 0 , and $+1$ charge states of V_{Na} and Na_i , where i means an interstitial, by taking into account the $+1$ oxidation state. In contrast, the oxidation states of pnictogen elements in typical III-V semiconductors are -3 , despite being -1 in MPn. Therefore, we computed the charge states for V_{P} from -1 to $+3$, and for P_i from -3 to $+1$. We modeled the vacancies at all inequivalent sites and an interstitial site (X_{il} , $X = \text{Na}, \text{P}$), which was initially located at the local minimum of the all-electron charge density shown in Fig. 1(d). We also calculated interstitial P located between the P–P bond because it was found to be stable in the 0 and -1 charge states using the ShakeNBreak code [42,43].

The calculations of the defect formation energies followed the general methodology [44]. The initial site symmetries were reduced by randomly displacing atoms

within 1.3 times the shortest bond length from the initial defect site by up to 0.2 \AA . The finite size errors in the defect formation energies were corrected using the extended Freysoldt-Neugebauer-Van de Walle scheme [45,46], which worked satisfactorily for various systems [26,47–52]. The dielectric constants were defined as the sum of the ion-clamped (ϵ_{∞}) and ionic (ϵ_{ion}) dielectric constants; they were evaluated using HSE06 and PBEsol [53], respectively, based on density functional perturbation theory [54,55]. The ϵ_{∞} and ϵ_{ion} values for o -NaP are (8.2, 5.7, 5.6) and (5.2, 8.9, 4.8), respectively. Perturbed host states were identified based on Ref. [16].

We constructed the chemical potential diagrams and convex hulls from the total energies of the competing phases using HSE06. The competing phases were obtained from the MPD [56].

Electron and hole capture coefficients were calculated for V_{P1} . We adopted the static approximation in conjunction with the one-dimensional CCDs developed by Alkauskas *et al.* [57]. The potential energy surfaces of the defects are mapped along the configuration coordinate between the equilibrium defect geometries for a given charge transition. We define the generalized configuration coordinate (Q) as $\sqrt{\sum_{\alpha} M_{\alpha} \cdot \Delta \mathbf{R}_{\alpha}^2}$, where M_{α} and $\Delta \mathbf{R}_{\alpha}$ are the atomic mass and the displacement vector from the equilibrium position of atom α , respectively. The defect energies along the configuration coordinates were corrected using the formalism described in Ref. [58]. The anharmonicity in the CCD was accounted for by interpolating and/or extrapolating the potential energy surfaces and solving the vibrational Schrodinger equation numerically using CarrierCapture.jl [59].

To evaluate the carrier capture coefficients, we need to quantify the e -ph coupling and overlap of the vibrational wavefunctions. The former were quantified by computing the slope of $\langle \psi_i | \partial H / \partial Q | \psi_j \rangle$ as a function of Q , where ψ_i and ψ_j are the initial and final eigenstates, respectively [57]. We computed them in the neutral charge state within the PAW formalism described in Ref. [60] using Nonrad [60].

To calculate the overlap of the vibrational wavefunctions, we first computed the potential energy surfaces of the different defect charge states. Within standard DFT approaches, electrons occupy the lowest-energy eigenstates during self-consistent calculations. Technically, one can control the occupancy of the defect levels located outside the band gap (for example, above the conduction band minimum) using constrained occupation techniques, but some noise may appear in the energy [59]. Therefore, we needed to extrapolate the potential energy surfaces in the regions where defect levels crossed the band edges in the supercell calculations [e.g., $Q > 7 \text{ amu}^{1/2} \text{ \AA}$ for V_{P1}^0 in Fig. 7(b)]. A quadratic fit worked well for the $-1/0$ transitions [Fig. 7(a)] due to the structural similarity, but not for the $0/+1$ transitions [Fig. 7(b)]. Because the functional

form for extrapolation was often unclear, we used a linear function to extrapolate and a spline function to interpolate for the 0/+1 transitions, respectively, and discussed the results in a semiquantitative manner.

All the VASP input settings were generated with the VISE code (version 0.6.6) [61], while the processing related to defects was done with PYDETECT [62].

C. Experimental details

NaP was synthesized by the reaction of Na melt and P vapor. In an Ar-filled glove box (O_2 and $H_2O < 1$ ppm), sodium (Na) metal (Nippon Soda Co., Ltd., Japan; purity, 99.95%) and grains of pure phosphate (P) (Kojundo Chemical Laboratory Co., Ltd., Japan; purity, 6N; grain size, 0.5–2 mm) were weighed in a molar ratio of Na : P = 1:1.06, which was a P-rich composition to compensate for loss of P due to evaporation. (When Na and P were heated at a ratio of 1:1, a Na-rich phase, Na_3P , was formed as a second phase.) Na and P were separately placed in boron nitride (BN) crucibles (Zikusu Industry Co., Ltd.; purity, 99.7%; 8.5 mm outer diameter; 6.5 mm inner diameter; 18 mm depth). The crucibles were subsequently sealed inside a stainless-steel container (SUS316; outer diameter, 12.7 mm; inner diameter, 10.7 mm; height, 80 mm) filled with Ar gas. In this container, the crucible containing P was placed on top, and the crucible containing Na was placed on the bottom. A schematic diagram of the reaction container and a detailed experimental procedure are described in Ref. [63]. The sealed container was heated at 873 K for 24 h using an electric furnace and then slowly cooled to room temperature. After heating, the crucible containing sample was taken from the container in the glove box, and its weight was measured to evaluate the formation of NaP. The obtained sample ingot was pulverized with an alumina mortar for powder XRD and optical absorption measurements. Note that the NaP powder is very reactive to moisture and quickly turns brown and is possibly flammable when exposed to air.

The crystalline phases of the products were identified by powder XRD using a powder diffractometer (RINT2200, Rigaku, Japan, $Cu K\alpha$, 40 kV, and 30 mA). The pattern was indexed with NaP reference: orthorhombic, $P2_12_12_1$ (19), $a = 0.6038(1)$, $b = 0.5643(1)$, $c = 1.0142(2)$ nm [27]. In the Ar-filled glove box, the powder sample was encapsulated in a holder with Kapton tape window. Optical absorption measurements of the NaP powder sample were conducted through diffuse reflection on a double beam spectrometer (U4000, Hitachi, Japan) equipped with a $BaSO_4$ -coated integrating sphere. The powder sample was filled on the SiO_2 glass holder and covered with a SiO_2 glass plate in the Ar-filled glove box. MgO powder was used as the white reference. The Kubelka-Munk formalism

was employed to transform the measured diffuse reflection, R_d , into $F(R_d)$, which was directly proportional to the absorption, α , as follows: $\alpha \propto F(R_d) = (1 - R_d)^2 / 2R_d$. The samples after the measurement were first washed with ethanol and then dissolved in distilled water.

ACKNOWLEDGMENTS

We are grateful for insightful discussions with F. Oba, N. Tsunoda, and Y. Nose. We also extend our gratitude to K. Yoshida and Y. Tachibana for their sample preparation. This study was financially supported by JSPS KAKENHI (Grant No. 22H01755) and the E-IMR project at IMR, Tohoku University.

-
- [1] W. Smith, Selenium, *Nature* **7**, 361 (1873).
 - [2] W. G. Adams and R. E. Day, V. The action of light on selenium, *Proc. R. Soc. London* **25**, 113 (1877).
 - [3] I. Hadar, T. Song, W. Ke, and M. G. Kanatzidis, Modern processing and insights on selenium solar cells: The world's first photovoltaic device, *Adv. Energy Mater.* **9**, 1802766 (2019).
 - [4] T. K. Todorov, S. Singh, D. M. Bishop, O. Gunawan, Y. S. Lee, T. S. Gershon, K. W. Brew, P. D. Antunez, and R. Haight, Ultrathin high band gap solar cells with improved efficiencies from the world's oldest photovoltaic material, *Nat. Commun.* **8**, 682 (2017).
 - [5] J. Yan, T. J. Savenije, L. Mazzarella, and O. Isabella, Progress and challenges on scaling up of perovskite solar cell technology, *Sustainable Energy Fuels* **6**, 243 (2021).
 - [6] W. Shockley and H. J. Queisser, Detailed balance limit of efficiency of p - n junction solar cells, *J. Appl. Phys.* **32**, 510 (1961).
 - [7] A. M. Ganose, J. Park, A. Faghaninia, R. Woods-Robinson, K. A. Persson, and A. Jain, Efficient calculation of carrier scattering rates from first principles, *Nat. Commun.* **12**, 2222 (2021).
 - [8] A. M. Ganose, D. O. Scanlon, A. Walsh, and R. L. Z. Hoyer, The defect challenge of wide-bandgap semiconductors for photovoltaics and beyond, *Nat. Commun.* **13**, 4715 (2022).
 - [9] C. Wang, S. Chen, J.-H. Yang, L. Lang, H.-J. Xiang, X.-G. Gong, A. Walsh, and S.-H. Wei, Design of I2–II–IV–VI4 semiconductors through element substitution: The thermodynamic stability limit and chemical trend, *Chem. Mater.* **26**, 3411 (2014).
 - [10] O. Madelung, *Semiconductors: Data Handbook* (Springer, Berlin, 2004).
 - [11] W. Shockley and W. T. Read, Statistics of the recombinations of holes and electrons, *Phys. Rev.* **87**, 835 (1952).
 - [12] N. Hall, Germanium rectifier characteristics, *Phys. Rev.* **83**, 228 (1951).
 - [13] R. D. Shannon, Revised effective ionic radii and systematic studies of interatomic distances in halides and chalcogenides, *Acta Crystallogr., Sect. A* **32**, 751 (1976).
 - [14] See the Supplemental Material at <http://link.aps.org/supplemental/10.1103/PRXEnergy.2.043002> for computational settings, calculated structure properties, exciton Rydberg

- energies, a series of band structures, density of states, and optical absorption spectra, local structures and eigenvalues of V_{P2} , and XRD pattern of α -NaP powder sample.
- [15] F. Emmerling and C. Röhr, Alkalimetall-Arsenide A_3As_7 und AA_s ($A = K, Rb, Cs$). Synthesen, Kristallstrukturen, Schwingungsspektren/Alkaline metal arsenides A_3As_7 and AA_s ($A = K, Rb, Cs$). Preparation, crystal structure, vibrational spectroscopy, *Z. für Naturforsch. B* **57**, 963 (2002).
 - [16] Y. Kumagai, N. Tsunoda, A. Takahashi, and F. Oba, Insights into oxygen vacancies from high-throughput first-principles calculations, *Phys. Rev. Mater.* **5**, 123803 (2021).
 - [17] Y.-T. Huang, *et al.*, Strong absorption and ultrafast localisation in NaBiS₂ nanocrystals with slow charge-carrier recombination, *Nat. Commun.* **13**, 4960 (2022).
 - [18] R. A. Street and N. F. Mott, States in the gap in glassy semiconductors, *Phys. Rev. Lett.* **35**, 1293 (1975).
 - [19] M. Kastner, Bonding Bands, Lone-pair bands, and impurity states in chalcogenide semiconductors, *Phys. Rev. Lett.* **28**, 355 (1972).
 - [20] M. Niemeyer, P. Kleinschmidt, A. W. Walker, L. E. Mundt, C. Timm, R. Lang, T. Hannappel, and D. Lackner, Measurement of the non-radiative minority recombination lifetime and the effective radiative recombination coefficient in GaAs, *AIP Adv.* **9**, 045034 (2019).
 - [21] H. T. Nguyen, S. C. Baker-Finch, and D. Macdonald, Temperature dependence of the radiative recombination coefficient in crystalline silicon from spectral photoluminescence, *Appl. Phys. Lett.* **104**, 112105 (2014).
 - [22] P. Azarhoosh, S. McKechnie, J. M. Frost, A. Walsh, and M. van Schilfgaarde, Research update: Relativistic origin of slow electron-hole recombination in hybrid halide perovskite solar cells, *APL Mater.* **4**, 091501 (2016).
 - [23] M. Kato, M. Nishiwaki, and H. Fujiwara, Very high oscillator strength in the band-edge light absorption of zincblende, chalcopyrite, kesterite, and hybrid perovskite solar cell materials, *Phys. Rev. Mater.* **4**, 035402 (2020).
 - [24] Y. Kumagai, Computational Screening of p -type transparent conducting oxides using the optical absorption spectra and oxygen-vacancy formation energies, *Phys. Rev. Appl.* **19**, 034063 (2023).
 - [25] W.-J. Yin and Y. Yan, The electronic properties of point defects in earth-abundant photovoltaic material Zn₃P₂: A hybrid functional method study, *J. Appl. Phys.* **113**, 013708 (2013).
 - [26] Y. Kumagai, M. Choi, Y. Nose, and F. Oba, First-principles study of point defects in chalcopyrite ZnSnP₂, *Phys. Rev. B* **90**, 125202 (2014).
 - [27] H. Georg, V. Schnering, and W. Hönle, Zur Chemie und Strukturchemie der Phosphide und Polyphosphide. 20. Darstellung, Struktur und Eigenschaften der Alkalimetall-monophosphide NaP und KP, *Z. Anorg. Allg. Chem.* **456**, 194 (1979).
 - [28] A. Kanevce, M. O. Reese, T. M. Barnes, S. A. Jensen, and W. K. Metzger, The roles of carrier concentration and interface, bulk, and grain-boundary recombination for 25% efficient CdTe solar cells, *J. Appl. Phys.* **121**, 214506 (2017).
 - [29] J. Coutinho, V. P. Markevich, and A. R. Peaker, Characterisation of negative- U defects in semiconductors, *J. Phys.: Condens. Matter* **32**, 323001 (2020).
 - [30] J. Nelson, *The Physics of Solar Cells* (Imperial College Press, London, 2022).
 - [31] M. Kastner, D. Adler, and H. Fritzsche, Valence-alternation model for localized gap states in lone-pair semiconductors, *Phys. Rev. Lett.* **37**, 1504 (1976).
 - [32] A. V. Kolobov, On the origin of p -type conductivity in amorphous chalcogenides, *J. Non-Cryst. Solids* **198**, 728 (1996).
 - [33] A. Alkauskas, C. E. Dreyer, J. L. Lyons, and C. G. V. de Walle, Role of excited states in Shockley-Read-Hall recombination in wide-band-gap semiconductors, *Phys. Rev. B* **93**, 201304 (2016).
 - [34] P. Makula, M. Pacia, and W. Macyk, How to correctly determine the band gap energy of modified semiconductor photocatalysts based on UV-vis spectra, *J. Phys. Chem. Lett.* **9**, 6814 (2018).
 - [35] P. E. Blöchl, Projector augmented-wave method, *Phys. Rev. B* **50**, 17953 (1994).
 - [36] G. Kresse and D. Joubert, From ultrasoft pseudopotentials to the projector augmented-wave method, *Phys. Rev. B* **59**, 1758 (1999).
 - [37] G. Kresse and J. Furthmüller, Efficient iterative schemes for *ab initio* total-energy calculations using a plane-wave basis set, *Phys. Rev. B* **54**, 11169 (1996).
 - [38] A. V. Krukau, O. A. Vydrov, A. F. Izmaylov, and G. E. Scuseria, Influence of the exchange screening parameter on the performance of screened hybrid functionals, *J. Chem. Phys.* **125**, 224106 (2006).
 - [39] A. Seidl, A. Görling, P. Vogl, J. A. Majewski, and M. Levy, Generalized Kohn-Sham schemes and the band-gap problem, *Phys. Rev. B* **53**, 3764 (1996).
 - [40] Z.-H. Cui, Y.-C. Wang, M.-Y. Zhang, X. Xu, and H. Jiang, Doubly screened hybrid functional: An accurate first-principles approach for both narrow- and wide-gap semiconductors, *J. Phys. Chem. Lett.* **9**, 2338 (2018).
 - [41] Y. Hinuma, G. Pizzi, Y. Kumagai, F. Oba, and I. Tanaka, Band structure diagram paths based on crystallography, *Comput. Mater. Sci.* **128**, 140 (2017).
 - [42] I. Mosquera-Lois, S. R. Kavanagh, A. Walsh, and D. O. Scanlon, ShakeNBreak: Navigating the defect configurational landscape, *J. Open Source Softw.* **7**, 4817 (2022).
 - [43] I. Mosquera-Lois, S. R. Kavanagh, A. Walsh, and D. O. Scanlon, Identifying the ground state structures of point defects in solids, *Npj Comput. Mater.* **9**, 25 (2023).
 - [44] Y. Kumagai, L. A. Burton, A. Walsh, and F. Oba, Electronic structure and defect physics of tin sulfides: SnS, Sn₂S₃, and SnS₂, *Phys. Rev. Appl.* **6**, 014009 (2016).
 - [45] Y. Kumagai and F. Oba, Electrostatics-based finite-size corrections for first-principles point defect calculations, *Phys. Rev. B* **89**, 195205 (2014).
 - [46] C. Freysoldt, J. Neugebauer, and C. V. de Walle, Fully *ab initio* finite-size corrections for charged-defect supercell calculations, *Phys. Rev. Lett.* **102**, 016402 (2009).
 - [47] Y. Kumagai, K. Harada, H. Akamatsu, K. Matsuzaki, and F. Oba, Carrier-induced band-gap variation and point defects in Zn₃N₂ from first principles, *Phys. Rev. Appl.* **8**, 014015 (2017).

- [48] T. Gake, Y. Kumagai, and F. Oba, First-principles study of self-trapped holes and acceptor impurities in Ga_2O_3 polymorphs, *Phys. Rev. Mater.* **3**, 044603 (2019).
- [49] N. Tsunoda, Y. Kumagai, M. Araki, and F. Oba, One-dimensionally extended oxygen vacancy states in perovskite oxides, *Phys. Rev. B* **99**, 060103 (2019).
- [50] N. Tsunoda, Y. Kumagai, and F. Oba, Stabilization of small polarons in BaTiO_3 by local distortions, *Phys. Rev. Mater.* **3**, 114602 (2019).
- [51] N. Tsunoda, Y. Kumagai, A. Takahashi, and F. Oba, Electrically benign defect behavior in zinc tin nitride revealed from first principles, *Phys. Rev. Appl.* **10**, 011001 (2018).
- [52] Y. Kumagai, N. Tsunoda, and F. Oba, Point defects and *p*-type doping in ScN from first principles, *Phys. Rev. Appl.* **9**, 034019 (2018).
- [53] J. P. Perdew, A. Ruzsinszky, G. I. Csonka, O. A. Vydrov, G. E. Scuseria, L. A. Constantin, X. Zhou, and K. Burke, Restoring the density-gradient expansion for exchange in solids and surfaces, *Phys. Rev. Lett.* **100**, 136406 (2008).
- [54] S. Baroni and R. Resta, *Ab initio* calculation of the macroscopic dielectric constant in silicon, *Phys. Rev. B* **33**, 7017 (1986).
- [55] M. Gajdoš, K. Hummer, G. Kresse, J. Furthmüller, and F. Bechstedt, Linear optical properties in the projector-augmented wave methodology, *Phys. Rev. B* **73**, 045112 (2006).
- [56] Anubhav Jain, Shyue Ping Ong, Geoffroy Hautier, Wei Chen, William Davidson Richards, Stephen Dacek, Shreyas Cholia, Dan Gunter, David Skinner, Gerbrand Ceder, Kristin A. Persson, Commentary: The materials project: A materials genome approach to accelerating materials innovation, *APL Mater.* **1**, 011002 (2013).
- [57] A. Alkauskas, Q. Yan, and C. G. V. de Walle, First-principles theory of nonradiative carrier capture via multiphonon emission, *Phys. Rev. B* **90**, 075202 (2014).
- [58] Y. Kumagai, Finite-size corrections for defect energetics in one-dimensional configuration-coordinate diagrams, *Phys. Rev. B* **107**, L220101 (2023).
- [59] S. Kim, S. N. Hood, and A. Walsh, Anharmonic lattice relaxation during nonradiative carrier capture, *Phys. Rev. B* **100**, 041202 (2019).
- [60] M. E. Turiansky, A. Alkauskas, M. Engel, G. Kresse, D. Wickramaratne, J.-X. Shen, C. E. Dreyer, and C. G. V. de Walle, Nonrad: Computing nonradiative capture coefficients from first principles, *Comput. Phys. Commun.* **267**, 108056 (2021).
- [61] Y. Kumagai, *VISE*, <https://github.com/kumagai-group/vise>
- [62] Y. Kumagai, *Pydefect*, <https://github.com/kumagai-group/pydefect>
- [63] S. Iwasaki, M. Hoshino, H. Morito, M. Kumagai, Y. Katsura, M. Jeem, M. Ono, J. Nishii, and M. Fujioka, Electric transport properties of NaAlB_{14} with covalent frameworks, *Inorg. Chem.* **61**, 4378 (2022).